Microporous and Mesoporous Materials 201 (2015) 210–218

Contents lists available at ScienceDirect

Microporous and Mesoporous Materials

journal homepage: www.elsevier.com/locate/micromeso

# Thermally induced phase transformation of Pb-exchanged LTA and FAU-framework zeolite to feldspar phases

A.S. Radosavljevic-Mihajlovic [a], A.S. Kremenovic [b], A.M. Dosen [a], J.Z. Andrejic [a,*], V.T. Dondur [c]

[a] Institute of Nuclear Science "Vinča", University of Belgrade, Belgrade, Serbia
[b] Faculty of Mining and Geology, Laboratory for Crystallography, University of Belgrade, Djusina 7, 11000 Belgrade, Serbia
[c] Faculty of Physical Chemistry, Studentski Trg 3, Belgrade, Serbia

ARTICLE INFO

*Article history:*
Received 28 July 2013
Received in revised form 7 April 2014
Accepted 27 August 2014
Available online 6 September 2014

*Keywords:*
Thermally induced transformation
Pb-feldspar$_{LTA}$
Pb-feldspar$_{FAU}$
Rietveld method
Microstructure

ABSTRACT

Thermally induced phase transformations of Pb-exchange LTA and FAU zeolites were from ambient temperature to 1300 °C. Both frameworks collapse into amorphous intermediate products after heating between 600 and 650 °C. Prolonged heating of the intermediate product over 1100 °C results in the formation of disordered Pb-feldspar$_{LTA}$ [$a$ = 8.414 (4) Å, $b$ = 13.048 (4) Å, $c$ = 7.169 (4) Å, $\beta$ = 115.35° (3)] and Pb-feldspar$_{FAU}$ [$a$ = 8.422 (4) Å, $b$ = 13.054 (4) Å, $c$ = 7.173 (4) Å, $\beta$ = 115.37° (3)] phases. The phase conversions within the investigated temperature range were followed by thermal (DTA, TGA, and DSC), XRPD, and Raman methods.



## 1. Introduction

The preparation of various aluminosilicate ceramic materials using synthetic zeolites as precursors has been a topic of great interest during the last three decades. This method of synthesis is often called the thermal-induced transformation of zeolite (ZTIT) and has certain advantages over other conventional methods [1–7]. The thermal treatment causes the collapse of the microporous zeolitic structure which leads to the formation of an amorphous phase, and subsequently, to the recrystallization of the more dense crystalline phases than the starting zeolite structure. The type and the valence of the extraframework cations cause the recrystallization of amorphous substances into different framework topologies. Therefore, the ZTIT method of synthesis could be considered as a novel route for the investigation of the three-component $MO-Al_2O_3-SiO_2$ (M = monovalent or divalent cation) phase systems as well.

The syntheses of aluminosilicate ceramics with thermally induced structural conversions of LTA- or FAU-framework zeolites in the system of $MAl_2Si_2O_8$ ($M = Ca^{2+}$, $Sr^{2+}$ or $Ba^{2+}$) are presented in literature [8–13]. To the best of our knowledge the synthesis by the ZTIT method of a feldspar with $Pb^{2+}$ as cation was reported only once almost 20 years ago [14]. It is well known, that feldspars are tectoaluminosilicate minerals with a general chemical formula $M[(Al,Si)_4O_8]$, where M represents alkali or alkali earth metal ions ($Na^+$, $K^+$, $Ca^{2+}$, $Ba^{2+}$) and other trace elements such as $Li^+$, $Rb^+$, $Sr^+$, $Mg^{2+}$, $Pb^{2+}$ [14–18]. Pure Pb-feldspar has not yet been found in nature. The Pb content is usually high in K-feldspars found in granites and syenites, where structural Pb can make up to more than 10% of the total whole-rock lead [19].

There are several different methods for the synthesis of the Pb-feldspar. Sorrell [20] synthesized Pb-feldspar *in situ* (from room temperature up to 1673 K) by solid-state reaction between kaolin-type clays and Ba, Sr and Pb sulfates. He reported that due to the similar nature of the potassium feldspar and lead feldspar they form an isomorphic mineral series. Bruno and Gazzoni [21] were the first to calculate the values of the unit cell of the Pb-feldspar obtained by the hydrothermal synthesis. Their result showed that during thermal treatment different temperatures cause the rearrangement in the Si/Al ordering of the Pb-feldspar. Further research showed that hydrothermally synthesized Pb-feldspar at a temperature of 520 °C shows some degree of order in the distribution of $Si^{4+}$ and $Al^{3+}$ in the structure (the unit cell parameter $c$ is close to 14 Å) [21]. As temperature increases to 1085 °C the disorder of the distribution of the Si/Al ratio increases (unit cell parameter $c$ is reduced to near 7 Å) [22]. Schell determined that well ordered Pb-feldspars crystallize in the $C2/m$ space group [23]. Benna et al. [24] synthesized the ordered ($I2/c$) and disordered ($C2/m$)

* Corresponding author.

http://dx.doi.org/10.1016/j.micromeso.2014.08.059
1387-1811/

Pb-feldspar by solid-state reaction. Based on their research, disordered lead feldspar has a "split Pb-site configuration", whereas the ordered structure has the Pb atom displaced further from the *c* glide plane. The cell parameters of the disordered and ordered Pb feldspar are significantly different, and in particular the *a* parameter seems to decrease as the ordering in the structure increases [24]. Rui et al. [25] proposed a new way of synthesizing the Pb-feldspar. The starting components for the experiment were: the natural K-feldspar and Pb $(NO_3)_2$ powders that were mixed together and annealed at 380 °C for 48 h and the obtained material had the desired quality. The results of the ion exchange method indicate that the alkali and alkali earth ions in feldspar could be replaced by the $Pb^{2+}$ cation. Steinike et al. [14] synthesized the Pb-feldspar from the Pb ion exchange LTA zeolite.

Nonetheless, systematic investigations with the aim of determining the optimal conditions for the synthesis of Pb cation exchanged zeolites ceramics of technological interest are very scarce [26]. The Pb-feldspars are synthesized from two kind zeolites topology, the LTA-zeolite with ratio Si:Al = 1:1 and high-silica FAU-zeolite with ratio Si:Al = 1:1.34. The main goal of this work is to observe the phase transformation of the Pb-exchanged LTA and FAU zeolites and to determine the crystal structures of the synthesized Pb-feldspar$_{LTA}$ and Pb-feldspar$_{FAU}$.

## 2. Experimental part

The calcium form of the LTA (Si/Al = 1.00) and sodium form of the FAU (Si/Al = 1.34) zeolite structure types [27], manufactured by Union Carbide Co., were used as starting materials. Fully exchanged $Pb^{2+}$ forms of these zeolites were prepared after several successive exchanges from 0.21 M $Pb(NO_3)_2$ solutions with the solid/liquid ratio (S/L) 1/30. The chemical composition of the samples was analyzed by an atomic absorption spectrophotometer (AAS), with a Perkin-Elmer 390 instrumental device. The presence of different cations was determined by EDAX analysis.

The thermal behavior of the Pb-exchanged zeolites was investigated by DTA/TG (different thermal and thermogravimetric analysis) using the Netzsch simultaneous analyzer; model STA-409 EP and DTA cells. Both zeolite precursors were analyzed at a heating rate of 10°/min. A Netysch-421 type furnace was used for the heating of the samples at temperatures over 700–1300 °C for 1 h.

The X-ray powder diffraction (XRPD) patterns were obtained on a Philips PW-1710 automated diffractometer Cu Kα, operated at 40 kV and 30 mA, with diffracted beam curved graphite monochromatic and a Xe-filled proportional counter.

The diffraction data of the thermally treated samples were collected in the range of 4–70° 2$\theta$ count time 1.0 s and a step size 0.02°, for routine phase analysis. For the Rietveld refinements data were collected by in the step-scanning mode in the range of 4–135° 2$\theta$ count time was increased to 12.5 s, and step size was 0.02°. Structural refinements were performed using the Rietveld method [28] implemented in the FullProf program [29,30]. The peak profiles were modeled using the Thompson–Cox–Hastings modified pseudo-Voigt (TCH-pV) function.

The X-ray line broadening was analyzed by the computer program Breadth [31]. This program calculates the microstructural parameters according to the Warren–Averbach and simplified integral breadth methods [32]. Input data for the Breadth program, unit-cell parameters, peak positions ($2\theta_{max}$) and Lorenz/Gauss mixing components ($\eta$), were taken from the output of the FullProf program. The X-ray line broadening of the $00l$ (2, 4,...10) and $0k0$ (2, 4,...10) reflections were analyzed.

Investigations of the crystal morphology of the thermally treated Pb-synthesized phases were analyzed with the scanning electron microscopy (SEM), using a JEOL 840A instrument. The samples were gold sputtered in a JFC 1100 ion sputtered. The chemical analyses of all samples were determined by EDAX.

Unpolarized Micro-Raman scattering measurements were performed in the backscattering configuration using Jobin Yvon T64000 spectrometer equipped with nitrogen cooled Symphony® charge-coupled-device detector (CCD). As an excitation source we used 514.5-nm line of $Ar^+/Kr^+$-ion laser operating at low power in order to avoid the heating of the sample.

## 3. Results and discussion

### 3.1. Chemical and thermal analysis

The AAS results of the chemical analysis of the ion exchanged Pb-zeolite are shown in the Table 1. These results show that the complete $Pb^{2+} \rightarrow Ca^{2+}$ for LTA and $Pb^{2+} \rightarrow Na^{+}$ exchanges on initial zeolites were achieved. Also, the EDAX results of the chemical analyses of the Pb-feldspar$_{LTA}$ and Pb-feldspar$_{FAU}$ are shown in Table 1.

Thermal stability (DTA and TGA) and crystal morphology (SEM) of fully exchanged Pb LTA- and FAU-framework zeolites obtained in the range from ambient temperature to 1000 °C are shown in Figs. 1 and 2.

Endothermic peaks at 159 °C for Pb-LTA and 132 °C for Pb-FAU, correspond to the loss of zeolitic water or their dehydration temperature [14]. Figs. 1a and 2a show the SEM images of Pb-LTA, FAU zeolites heated at 200 °C for 1 h. The main morphological feature of Pb-exchanged zeolite at this temperature is the presence of the cubic crystal forms. The second endothermic peak ~500 °C for both Pb-zeolite frameworks are corresponding to loss of structural water. According the literature data at temperature 530 °C, the strong influence of water molecules on the lead cations, leads to change of framework symmetry of Pb-LTA zeolite [14]. The process of dehydration is complete above 600 °C, and it corresponds to a 15% weight loss.

In fact, the small broad exothermic effect recorded at 628° and 618 °C, for zeolite Pb-LTA and Pb-FAU respectively, can be related to the final breakdown of their almost completely dehydrated microporous zeolitic structure with the consequent formation of more compact, amorphous phases. Rounded crystal forms (Fig. 1b and 2b) correspond to the appearance of the amorphous phase in both samples.

The DTA curve (Figs. 1 and 2) shows well-formed strong exothermic peaks at 770 °C for Pb-LTA and 755 °C for Pb-FAU zeolite, respectively. These peaks represent the temperature of crystallization of a new feldspar phase. After heating at 800 °C for 1 h the

**Table 1**
Chemical analyses (% wt) of phases synthesized from Pb-exchanged LTA- and FAU-framework zeolites as initial materials.

| Oxide (%) | $SiO_2$ | $Al_2O_3$ | PbO | $Na_2O$ | CaO | Σ |
|---|---|---|---|---|---|---|
| AAS method | | | | | | |
| Dehydrated[a] Pb-LTA | 33.05 | 31.37 | 35.57 | – | 0.012 | 99.99 |
| Dehydrated[a] Pb-FAU | 38.13 | 27.83 | 34.00 | 0.03 | – | 100.00 |
| Pb-feldspar$_{LTA}$ | 33.10 | 31.39 | 35.54 | – | – | 100.03 |
| Pb-feldspar$_{FAU}$ | 38.10 | 27.85 | 34.05 | – | – | 100.00 |
| Element (%) | Si | Al | Pb | Na | Ca | O |
| EDAX method | | | | | | |
| Pb-LTA | 15.35 | 14.34 | 32.7 | – | – | 37.61 |
| Pb-FAU | 17.82 | 13.00 | 31.8 | | | 37.38 |
| Pb-feldspar$_{LTA}$ | 15.30 | 14.38 | 31.84 | | | 37.58 |
| Pb-feldspar$_{FAU}$ | 17.80 | 12.95 | 31.9 | | | 37.35 |

[a] The water contents of hydrated Pb-exchanged LTA- and FAU-framework zeolites are determined from TGA analyses as 17.72% and 25.6%, respectively.

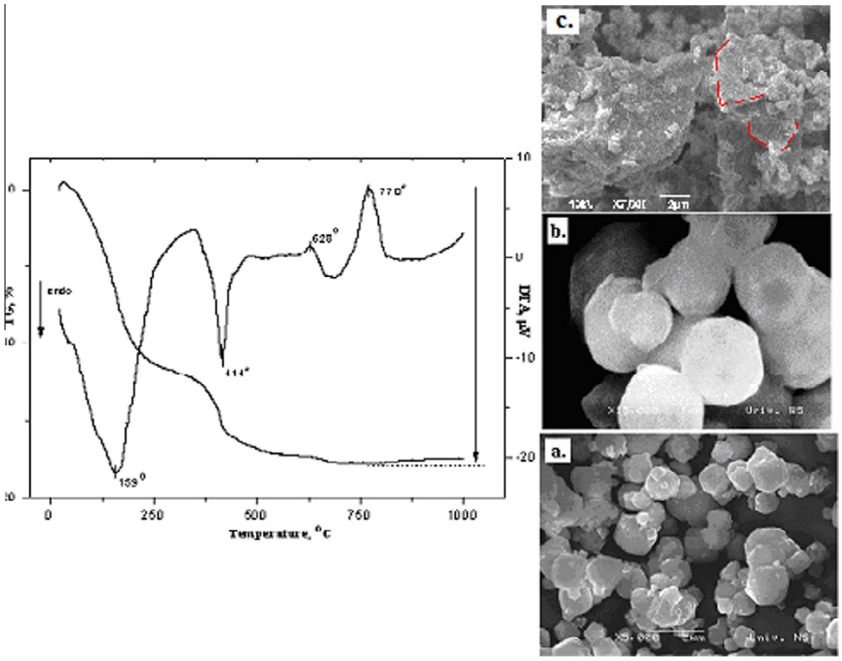


**Fig. 1.** The thermal (DTA/TG) curves and SEM photographs of observed Pb-exchange LTA-framework zeolite; (a) the SEM image of thermal treated Pb-LTA at 200 °C/1 h; (b) the SEM image of thermal treated Pb-LTA at 650 °C/1 h; (c) the SEM image of thermal treated Pb-LTA at 800 °C/1 h.

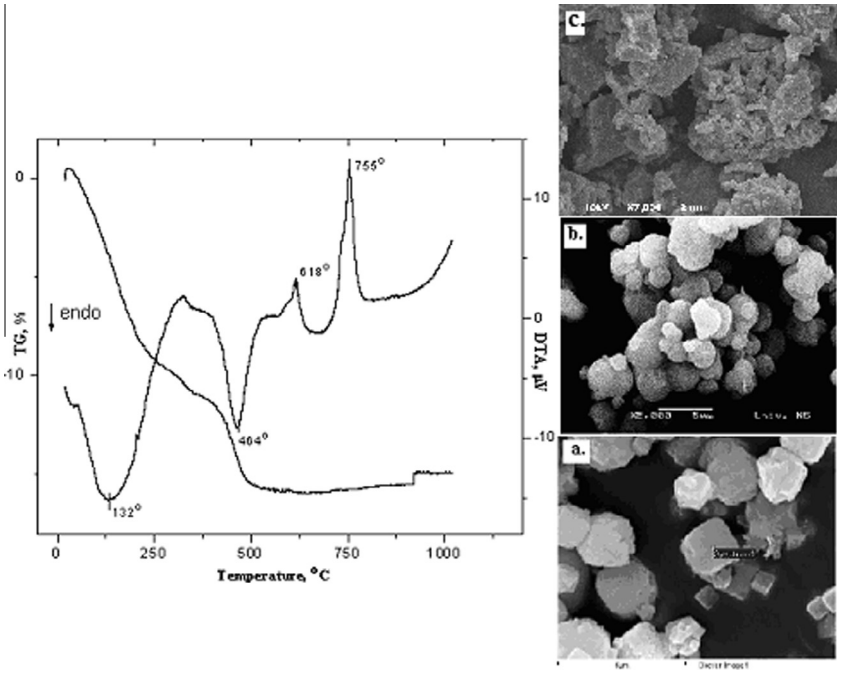


**Fig. 2.** The thermal (DTA/TG) curves and SEM photographs of observed Pb-exchange FAU-framework zeolite; (a) the SEM image of thermal treated Pb-FAU at 200 °C/1 h; (b) the SEM image of thermal treated Pb-FAU at 650 °C/1 h; (c) the SEM image of thermal treated Pb-FAU at 800 °C/1 h.

observed zeolite crystals are morphologically different and have changed into round grain forms shown in Figs. 1c and 2c.

The XRPD investigations of the phase conversions of the Pb-exchanged LTA- and FAU framework zeolites, in the temperature range from ambient up to 1300 °C shown in Fig. 3(a and b) were carried out on the samples chosen with reference to results of the thermal measurements presented in this paper.

According to the literature data [1–13], the ZTIT process can be roughly schematized into three stages. The first step corresponds to the dehydration process, the increase of cation diffusion, and rearrangement of $Pb^{2+}$ cations from the zeolite cages. After the complete dehydration of the Pb-LTA and Pb-FAU zeolites the tetrahedral T–O–T bridges collapse simultaneously with the collapse of the zeolite structure. From the thermal curves and XRPD patterns (Figs. 1, 2, 3a and 4a) the observed dehydration processes of the Pb-exchange LTA and FAU framework zeolites are equally distinct. The zeolite structures are transformed into amorphous intermediate products with the increasing temperature of

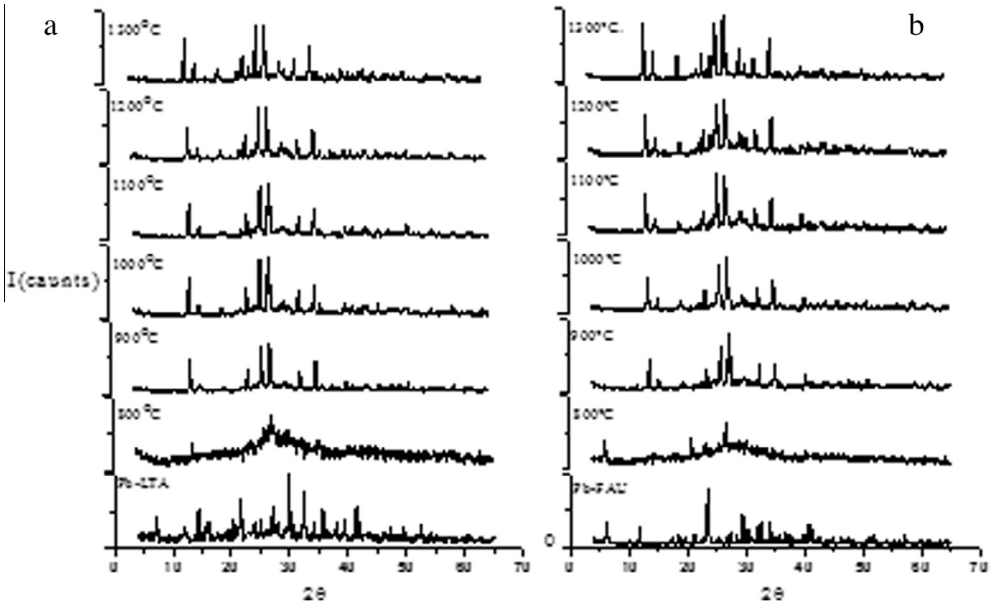


**Fig. 3.** (a) Comparative XRPD patterns of thermally treated Pb-LTA zeolite in temperature range 800–1200 °C; (b) Comparative XRPD patterns of thermally treated Pb-FAU zeolite in temperature range 800–1200 °C.

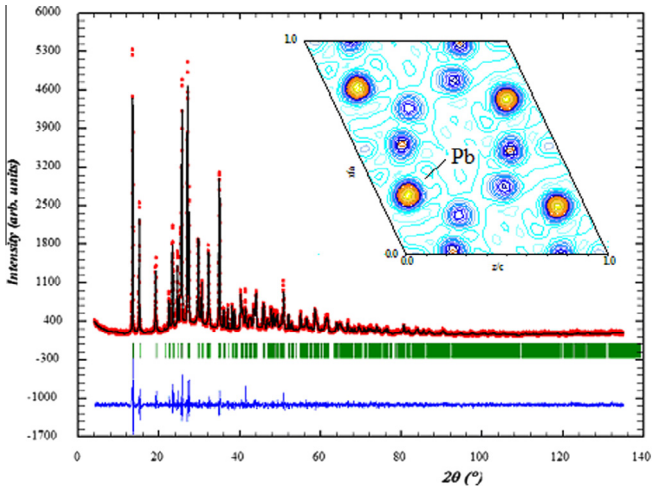


**Fig. 4.** Rietveld refinement plot of Pb-feldspar$_{LTA}$ (in a graphic is presented the Fourier different map, the electron density around the Pb site).

annealing. The second step involves the processes of the structural reorganization of (Si, Al) $O_4$ tetrahedra and/or secondary building units that occur in the amorphous intermediate product. It is well known from the abundant literature data [1–13] that the framework of the cation exchanged zeolites collapses during heating between 400 and 850 °C. The formation of an amorphous substance of Pb-LTA and Pb-FAU zeolites started approximately between 615 and 630 °C, (Figs. 1b, 2b, 3b and 4b), and the final stage of this thermal conversion includes the polymorphous transformation into more stable crystalline phases, Pb-feldspar$_{LTA}$ and Pb-feldspar$_{FAU}$. It is well known, that during the ZTIT processes (increasing temperature/time conditions) a diphyllosilicate topology precedes the feldspar topology [8,9]. However it is not always the case. The results show that this phenomenon is not observed in zeolite modified with $Ca^{2+}$[8] and $Pb^{2+}$. The feldspar phases formed from both zeolite precursors are stable at temperatures from 900 to 1300 °C, Figs. 3 and 4. The change of unit-cell parameters during

**Table 2**
The unit cell parameters of Pb-feldspar$_{LTA}$ and Pb-feldspar$_{FAU}$ during the thermal treatments (*ex-situ* measurements).

| $T$ (°C) | $a$ (Å) | $b$ (Å) | $c$ (Å) | $V$ (Å$^3$) |
|---|---|---|---|---|
| Pb-feldspar$_{LTA}$/space group $C2/m$ | | | | |
| 900 | 8.387 (3) | 13.043 (2) | 7.157 (2) | 708.09 (4) |
| 1000 | 8.392 (2) | 13.043 (2) | 7.159 (3) | 709.00 (3) |
| 1100 | 8.414 (1) | 13.048 (2) | 7.169 (3) | 710.80 (2) |
| 1200 | 8.427 (3) | 13.047 (2) | 7.165 (3) | 710.89 (2) |
| Pb-feldspar$_{FAU}$/space group $C2/m$ | | | | |
| 900 | 8.390 (3) | 13.032 (3) | 7.162 (4) | 708.51 (4) |
| 1000 | 8.406 (3) | 13.026 (2) | 7.163 (3) | 709.00 (2) |
| 1100 | 8.422 (4) | 13.054 (4) | 7.173 (2) | 711.36 (2) |
| 1200 | 8.429 (2) | 13.055 (2) | 7.175 (2) | 711.89 (2) |

the thermal treatment (*ex-situ* measurements) of the investigated samples of Pb-feldspar$_{LTA}$ and Pb-feldspar$_{FAU}$ are presented in Table 2.

The unit-cell parameters of both Pb-feldsparLTA and Pb-feldsparFAU phases vary slightly with the change of temperature. Such variations are noticeable along the *a*-axis and *b*-axis (Table 2). Previous researches has noted that the presence of $Pb2^+$ cations in the structure of feldspar leads to significant deviations of the unit cell parameters [22,23]. The changes in *a*-axis and volume of unit cell are related to the Al–Si ordering in Pb-feldspars [33]. The anomalous behavior of the *b*-axis during the thermal treatment was reported by Tribaudino et al. [33]. This phenomenon is explained by considering the OA1–OA1 shared edge between Pb-centered polyhedra, through which Pb atoms are facing. Changes in unit cell parameters for obtained Pb-feldspars phases are consequence of the degree of ordering in the structures during the thermal treatment.

### 3.2. Rietveld refinements of Pb-feldspar$_{LTA}$ and Pb-feldspar$_{FAU}$

The main problem in refining these feldspar structures was the Al/Si ordering scheme and the effects of substitution of different non-tetrahedral cations [16,22]. Most feldspar crystallized with a disordered distribution of $Si^{4+}$ and $Al^{3+}$ in the space group $C2/m$. The process of the structure ordering into space group $I2/c$ is slow

**Table 3**
Selected results from Rietveld refinements for Pb-feldspar$_{LTA}$ and Pb-feldspar$_{FAU}$.

| | Pb-feldspar$_{LTA}$ | Pb-feldspar$_{FAU}$ |
|---|---|---|
| Number of measured point | 6546 | 6745 |
| Profil function | TCH Pseudo-Voigt | |
| *a* (Å) | 8.414 (4) | 8.4220 (4) |
| b (Å) | 13.048 (4) | 13.054 (4) |
| c (Å) | 7.169 (5) | 7.173 (5) |
| *β* (°) | 115.358 (3) | 115.37 (3) |
| *V* (Å$^3$) | 711.35 (2) | 712.60 (2) |
| *U* | 0.0233 (3) | 0.0232 (3) |
| *Y* | 0.0531 (4) | 0.0427 (2) |
| *X* | 0.0157 (3) | 0.0152 (4) |
| *Asy* 1 | 0.1135 (3) | 0.0940 (3) |
| *Asy* 2 | 0.0269 (3) | 0.0286 (3) |
| *Chi2* | 2.07 | 2.08 |
| $R_{wp}$ | 17.6 | 18.6 |
| $R_p$ | 17.5 | 18.6 |
| *R* (*F*) | 6.39 | 6.91 |
| *R* (*B*) | 4.68 | 4.59 |

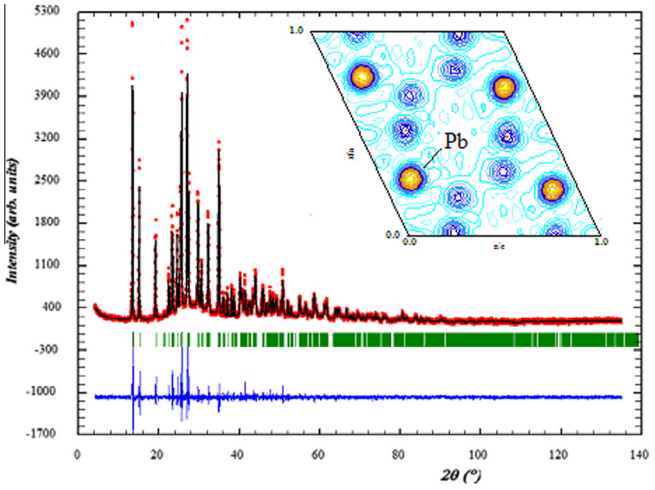


**Fig. 5.** Ritveld refinement plot of Pb-feldspar$_{FAU}$ (in a graphic is presented the Fourier different map, the electron density around the Pb site).

and difficult. The crystal structures of ordered (*I*2/*c*) and disordered Pb-feldspars (*C*2/*m*) have been determined [24]. The main difference between these two feldspars is in the number and the intensity of the *b*-type ($h + k = 2n + 1$, $l = 2n + 1$) superstructure reflections. Tribaudino et al. [33] concluded that the *b*-type superstructure reflections in the monoclinic *I*2/*c* feldspars are due to the displacement of the non-tetrahedral cations. It was reported that the increasing of annealing temperature induces a significant decrease of the intensity of the *b*-type reflections in the structure of the Pb-feldspar [34]. The disordered Pb-feldspar is characterized by a completely disordered arrangement of atoms Al and Si and in this structure the average Pb-position moves toward the *c* plane. The physical–chemical properties of the $Pb^{2+}$ may influence both the stability of ordered and disordered configurations and the kinetics of Al, Si diffusion, and thus explains the anomalous behavior of the Pb-feldspar [24].

In this research, the reflections of the "*b*" type are not found, so the crystal structures of both Pb-feldspars were refined by the Rietveld method in the C2/*m* space group. The cell parameters and agreement factors for both refinements are given in the Table 3.

After the refinement of the feldspar structure with the Pb cation positioned on the mirror plane (*x*, 0, *z*), the Fourier map showed an anomalous electron-density distribution around the Pb site, Figs. 5 and 6. This indicates the Pb-atoms are arranged in the two split positions, 4*i* on the plane *m* and general position 8*j* with coordinates (*x*, *y*, *z*). The final Rietveld models of agreement of the calculated and measured intensities are presented in Figs. 4 and 5.

The refined fractional coordinates, atomic displacement parameters and site occupation factors (SOF) are presented in Tables 4 and 5.

In the "ideal" feldspar structure [space group *C*2/*m*, axis *c* ~7 Å] the atoms ($K^+$, $Ba^{2+}$ or $Ca^{2+}$), $O_{A1}$ and $O_{A2}$ are located on the plane of symmetry *m* (4*i*) [16]. In the structure of $Pb_{0.92}Al_2Si_2O_8$ and $Pb_{0.88}Al_2Si_2O_8$, were the axis *c* is 7.169 and 7.173 Å respectively, the Pb cations are shifted to the general position 8*j*. The oxygen $O_{A1}$ is shifted to a twofold axis and oxygen $O_{A2}$ remains on the plane of symmetry *m*. Selected values for the interatomic distances for both Pb-feldspars are presented in Table 6. The coordination polyhedra for Pb cations are presented in the Fig. 7.

The starting Si/Al ratios in the ion exchanged zeolites are Si:Al = 1:1 for the Pb-LTA and Si:Al = 1:1.25 for the Pb-FAU. The average interatomic T–O distance (if we ignore the impact of the cations) is 1.675 for the 1:1 ratio and 1.667 Å for the 1:1.25 ratio (for $O^{-2}$ in coordination II) calculated based on the literature data [35]. The average ⟨T–O⟩ distance in the structure of the Pb-feldspar$_{LTA}$ is 1.661 and shows little deviation from the calculated values for the Si:Al = 1:1 ratio in the tetrahedral network. The average ⟨T–O⟩ distance in the structure of the Pb-feldspar$_{FAU}$ is 1.667 and it is close to the calculated values. During the process of the thermally induced transformation of the Pb-zeolites a stable feldspar framework forms with the random distribution of Si/Al in the tetrahedral position. Deviations that are present are probably due to the influence of the Pb cations on the feldspar structure.

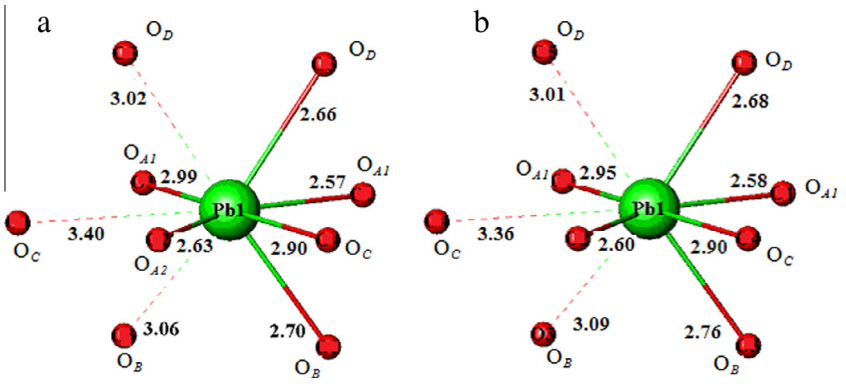


**Fig. 6.** The coordination sphere around the Pb cation (a) in Pb-feldspar$_{LTA}$ and (b) Pb-feldspar$_{FAU}$ (The atoms of oxygen are presented with red ball). (For interpretation of the references to color in this figure legend, the reader is referred to the web version of this article.)

**Table 4**
Atomic coordinates (*x*, *y*, *z*), site occupation factors (SOF) and atomic displacement parameters ($B_{iso}$) for Pb-feldspar$_{LTA}$.

| Atom | *x* | *y* | *z* | $B_{iso}$ (Å$^2$) | SOF |
|---|---|---|---|---|---|
| Pb | 0.2734 (2) | 0.0239 (4) | 0.1393 (2) | 2.308 (3) | 0.475 (4) |
| T1 | 0.0036 (2) | 0.1775 (4) | 0.2271 (9) | 0.563 (3) | 0.5 |
| T2 | 0.6919 (2) | 0.1138 (4) | 0.3491 (9) | 0.563 (3) | 0.5 |
| $O_{A1}$ | 0.0000 | 0.1410 (1) | 0.0000 | 4.837 (4) | 0.5 |
| $O_{A2}$ | 0.6164 (3) | 0.0000 | 0.2945 (1) | 2.349 (3) | 0.5 |
| $O_B$ | 0.8220 (3) | 0.1266 (2) | 0.2211 (2) | 4.821 (6) | 1.0 |
| $O_C$ | 0.0199 (3) | 0.3066 (2) | 0.2544 (2) | 1.208 (6) | 1.0 |
| $O_D$ | 0.1855 (2) | 0.1247 (9) | 0.4048 (2) | 0.842 (6) | 1.0 |

**Table 5**
Atomic coordinates (*x*, *y*, *z*), site occupation factors (SOF) and atomic displacement parameters ($B_{iso}$) for Pb-feldspar$_{FAU}$.

| Atom | *x* | *y* | *z* | $B_{iso}$ (Å$^2$) | SOF |
|---|---|---|---|---|---|
| Pb | 0.2750 (2) | 0.0218 (4) | 0.1405 (2) | 2.534 (3) | 0.45 (4) |
| T1 | 0.0038 (2) | 0.1772 (3) | 0.2297 (2) | 0.046 (3) | 0.5 |
| T2 | 0.6956 (2) | 0.1167 (2) | 0.3482 (1) | 0.046 (3) | 0.5 |
| $O_{A1}$ | 0.00000 | 0.1378 (1) | 0.00000 | 4.837 (4) | 0.5 |
| $O_{A2}$ | 0.6147 (3) | 0.00000 | 0.2945 (1) | 2.160 (3) | 0.5 |
| $O_B$ | 0.8183 (3) | 0.1290 (2) | 0.2235 (2) | 3.225 (1) | 1.0 |
| $O_C$ | 0.0181 (3) | 0.3066 (2) | 0.2539 (2) | 2.458 (1) | 1.0 |
| $O_D$ | 0.1868 (2) | 0.1261 (3) | 0.4047 (2) | 1.964 (2) | 1.0 |

**Table 6**
Selected interatomic distances in Å for both feldspars. T represents Si or Al.

| | Pb-feldspar$_{LTA}$ | Pb-feldspar$_{FAU}$ |
|---|---|---|
| ⟨$T_1$–O⟩ | 1.672 | 1.682 |
| ⟨$T_2$–O⟩ | 1.650 | 1.650 |
| ⟨T–O⟩ | 1.661 | 1.666 |
| ⟨T–O–T⟩ | 141.351 | 139.779 |
| Pb–$O_{A1}$ | 2.579 (2) | 2.583 (2) |
| Pb–$O_{A1}$ | 2.991 (2) | 2.953 (2) |
| Pb–$O_{A2}$ | 2.629 (2) | 2.603 (1) |
| Pb–$O_B$ | 2.708 (1) | 2.763 (2) |
| Pb–$O_B$ | 3.066 (1) | 3.090 (2) |
| Pb–$O_C$ | 3.400 (2) | 3.36 (2) |
| Pb–$O_C$ | 2.900 (1) | 2.906 (2) |
| Pb–$O_D$ | 2.665 (2) | 2.684 (1) |
| Pb–$O_D$ | 3.023 (1) | 3.012 (2) |
| ⟨Pb–O⟩ | 2.885 | 2.884 |

The site occupation factors for both feldspars were refined (Tables 4 and 5). From the refined values, it could be seen that both Pb-feldspars are characterized with site vacancies in the Pb positions. The mean Pb–O distance is longer than the distance, which is calculated from ionic radii sum from the literature data – 2.61 Å [32]. For celsian feldspar, Skellern [36] showed that for two vacant celsians, mean Ba–O distance was shorter for the sample, which had a smaller amount of vacancies. Grundy [37] calculated the Sr–O distance to be 2.82 Å for the vacant Sr-feldspar. This indicates that vacancies in the Sr positions affect the Sr–O distance. Deviations from the calculated values for both Pb-feldspars are present for the bond lengths of Pb–$O_{A1}$ ~ 2.99; Pb–$O_B$ ~ 3.08; Pb–$O_C$ ~ 3.4; Pb–$O_D$ ~ 3.00 Å. One explanation for the longer bond distance is derived from the presence of the $6s^2$ lone pair and the second explanation is the presence of vacancies in Pb site [34].

The coordination number of the extraframework cations in the feldspar structure is C.N = 9. To determine the coordination number of the Pb-feldspar the bond valence method (or bond valence sum) was used. This is a popular method to estimate the oxidation states and coordination geometries of atoms [38]. In the Table 7 we presented the average distances of M–O (M = $Ba^{2+}$, $Sr^{2+}$, $Pb^{2+}$) and bond valence sums for the different feldspar [24,39,40].

The bond-valence sums range from 1.80 to 2.0 v.u (valence unit), which is in good agreement with $2^+$ formal charges [41]. For both Pb-feldspars, the value for the bond valence sum $\sum v_{ij}$-M is approaching the ideal values, Fig. 6. Small deviations are present which is most likely the result of the distortion of the Pb polyhedra.

Calculated data for the bond valence sum $\sum v_{ij}$-$M^{VII}$, C.N = 7 showed low values of 1.21 for Pb-feldspar$_{LTA}$ and 1.18 for Pb-feldspar$_{FAU}$. This suggests that one should take into account all 9 oxygen atoms, which means that the C.N = 9. Evidently, in the investigated feldspars the two longer distances ⟨Pb–O⟩ (for Pb-feldspar$_{LTA}$ 3.40 and 3.06 Å; for Pb-feldspar$_{FAU}$ 3.36 and 3.09 Å) contribute to the bond valence sum.

### 3.3. Microstructure parameter of Pb-feldspar$_{LTA}$ and Pb-feldspar$_{FAU}$

The size-strain X-ray diffraction line broadening is used for the investigation of the strain and size of crystallites. In the disordered feldspar the structure has a random set of faults on planes with zone axis [001] whose slip vector has a component *c*/2 [42]. Nedić [10] showed that vacancies in Sr-feldspar were the cause of the X-ray line broadening and that the distribution of vacancies should be the highest in [001] direction. Microstructural parameters in Pb-feldspars were obtained using the Warren–Averbach and simplified integral breadth method. The results of micro-strain and size parameters, for surface-weighted ⟨$D_S$⟩ and volume-weighted ⟨$D_V$⟩ are showed in Table 8.

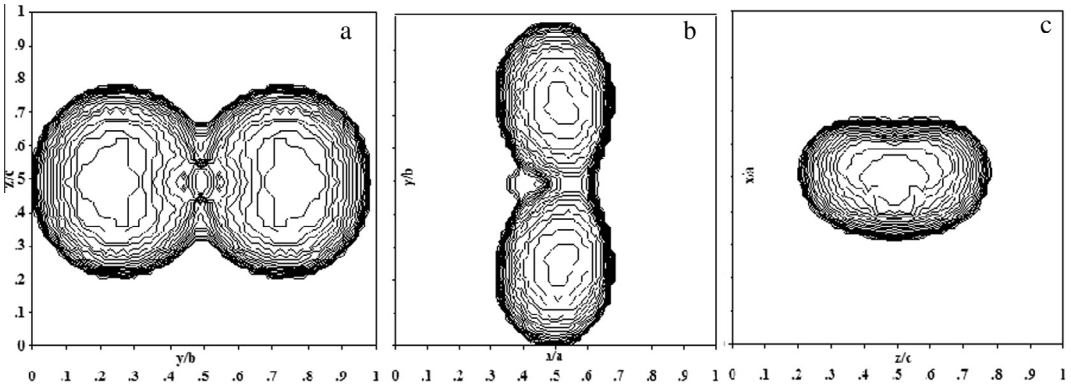


**Fig. 7.** The different projections in plane of three-dimensional body that represents apparent strain influence on the XRPD line broadening in Pb-feldspar$_{LTA}$; (a) the projection in plan *bc*, (b) the projection in plane *ab*, (c) the projection in plane *ca*.

**Table 7**
The bond distance M–O [M = $Pb^{2+}$, $Sr^{2+}$, $Ba^{2+}$] and bond valence sums ($\sum v_{ij}$) for some Pb, Sr and Ba feldspars.

| Sample | Pb-feldspar$_{LTA}$ $Pb_{0.92}Al_2Si_2O_8$ | Pb-feldspar$_{FAU}$ $Pb_{0.88}Al_8Si_2O_8$ | Pb-feldspar [20] $PbAl_2Si_2O_8$ | Sr-feldspar [29] $SrAl_2Si_2O_8$ | Ba-feldspar [28] $BaAl_2Si_2O_8$ |
|---|---|---|---|---|---|
| Space group | *C2/m* | *C2/m* | *I2/c* | | *I2/c* |
| $\langle^{VII}M–O\rangle$ | 2.791 | 2.761 | 2.718 | 2.682 | 2.862 |
| $\langle^{IX}M–O\rangle$ | 2.887 | 2.871 | 2.836 | 2.792 | 2.923 |
| $\sum v_{ij}$-$M^{VII}$ | 1.21 | 1.18 | | | |
| $\sum v_{ij}$-$M^{IX}$ | 2.1 | 2.2 | 2.35 | 1.812 | 1.87 |

**Table 8**
The microstructure parameters calculated from the XRPD data according to the Rietveld, Warren–Averbach and simplified integral breadths methods for samples Pb-feldspar$_{LTA}$ and Pb-feldspar$_{FAU}$.

| | Pb-feldspar$_{LTA}$ | | Pb-feldspar$_{FAU}$ | |
|---|---|---|---|---|
| *hkl* | 00*l* | 0*k*0 | 00*l* | 0*k*0 |
| Warren–Averbach method | | | | |
| $a'^3$ (Å) | 28.9 | 29.3 | 30.3 | 22.6 |
| $\langle D_S\rangle$ (Å) | 403 ± 1 | 462 ± 1 | 414 ± 1 | 530 ± 3 |
| $\langle D_V\rangle$ (Å) | 425 ± 3 | 447 ± 4. | 392 ± 2 | 470 ± 6. |
| $\langle\varepsilon^2\rangle^{1/2}\langle D\rangle_{S/2} \times 10^{-3}$ | 0.3 ± 0.08 | 0.32 ± 0.06 | 0.18 ± 0.005 | 0.18 ± 0.11 |
| $\langle\varepsilon^2\rangle^{1/2}\langle D\rangle_{V/2} \times 10^{-3}$ | 0.65 ± 0.02 | 0.82 ± 0.02 | 0.44 ± 0.136 | 0.2 ± 0.2 |
| $\langle\varepsilon^2\rangle^{1/2}_{a'/3} \times 10^{-3}$ | 0.24 ± 0.07 | 0.32 ± 0.05 | 017 ± 0.55 | 0.17 ± 0.11 |
| $\langle\varepsilon^2\rangle^{1/2}_{Gauss} \times 10^{-3}$ | 0.9 ± 0.01 | 0.12 ± 0.13 | 0.63 ± 0.83 | 0.17 ± 0.2 |
| Simplified integral-breadth methods | | | | |
| $\langle D\rangle_{CC}$ (Å) | 415 | 451 | 473 | 598 |
| $\langle D\rangle_{CG}$ (Å) | 426 | 447 | 471 | 481 |
| $\langle D\rangle_{GG}$ (Å) | 425 | 447 | 471 | 461 |
| $\langle\varepsilon^2\rangle^{1/2}_{CC} \times 10^3$ | 0.60 | 0.67 | 0.26 | 0.172 |
| $\langle\varepsilon^2\rangle^{1/2}_{CG} \times 10^3$ | 0.12 | 0.32 | 0.17 | 0.206 |
| $\langle\varepsilon^2\rangle^{1/2}_{GG} \times 10^3$ | 0.53 | 0.45 | 0.22 | 0.250 |
| FullProf | | | | |
| | *hkl* | | *hkl* | |
| Average apparent size (Å) | 674 (2) | | 1094 (2) | |
| Average mixing strain $\times 10^3$ (Å) | 1.513 (5) | | 2.50 | |

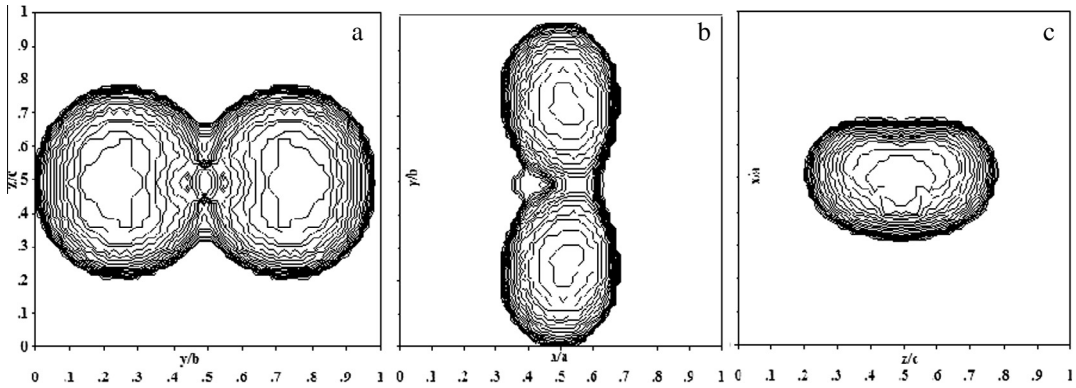


**Fig. 8.** The different projections in plane of three-dimensional body that represents apparent strain influence on the XRPD line broadening in Pb-feldspar$_{LTA}$; (a) the projection in plan *bc*, (b) the projection in plane *ab*, (c) the projection in plane *ca*.

The volume-averaged domain sizes evaluated from the simplified integral-breadth method in the approximation of Cauchy–Cauchy $\langle D\rangle_{CC}$, Cauchy–Gauss $\langle D\rangle_{CG}$, and Gauss–Gauss $\langle D\rangle_{GG}$ distribution of crystallites and strains are also given. The upper limits of strain from the simplified integral-breadth methods in the approximate Cauchy–Cauchy $\langle\varepsilon^2\rangle^{1/2}_{CC}$, Cauchy–Gauss $\langle\varepsilon^2\rangle^{1/2}_{CG}$ and Gauss–Gauss $\langle\varepsilon^2\rangle^{1/2}_{GG}$ distribution of crystallites and strains are also shown.

The crystallite size and strain parameters measured in the direction [00*l*] and [0*k*0] showed very similar values, according to the Warren–Averbach method. Surface-weighted $\langle D_S\rangle$ and volume-weighted $\langle D_V\rangle$ crystallite size parameters in the [00*l*] direction have the smallest values. The graphic presentations of XRPD line broadening due to the finite strain and size are shown in Figs. 7 and 8.

Variations of the microstructural parameters are in direct consequence of the degree of order in the structure of both feldspars. The most visible change is in the direction of crystallographic *b*-axis, which is sensitive to changes in bond lengths OA1–OA1 and to the ratio Si/Al in the structure. Differences in average apparent size and strain are due to the degree ordering of observed structures.

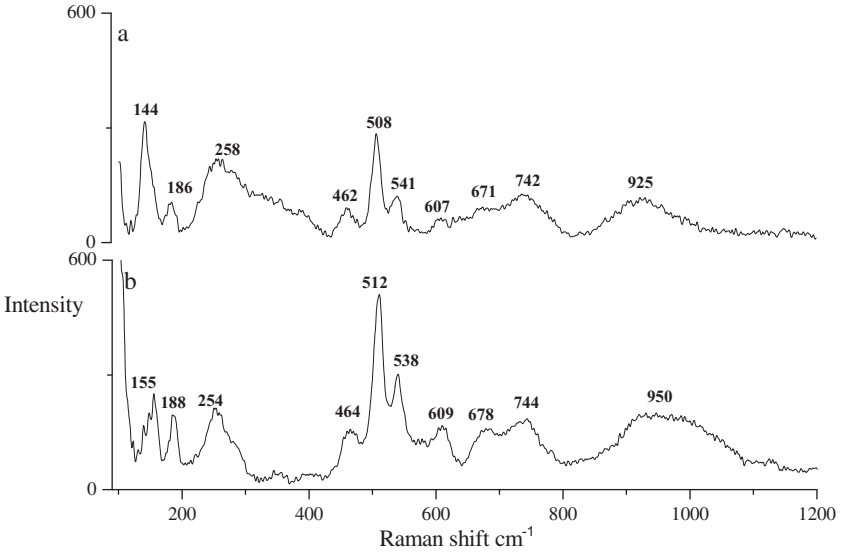


**Fig. 9.** The Raman spectra of the (a) Pb-feldspar$_{LTA}$ and (b) Pb-feldspar$_{FAU}$.

### 3.4. Raman spectroscopy

The comparative Raman spectra of the thermally treated (1200 °C/5 h) Pb-feldspar$_{LTA}$ and Pb-feldspar$_{FAU}$ are presented in the Fig. 9(a and b).

The structural factors, such as the wide distribution of the T–O–T bond angles, bond angle distortion in $SiO_4$ tetrahedral and the cation type and arrangement have significantly influenced the Raman spectra. Comparing the Raman spectras of both feldspars it is showed that the modes at frequencies of 508 and 541 cm$^{-1}$ (Fig. 9a), and 512 and 538 cm$^{-1}$ (Fig. 9b) are dominant in both spectra. This vibration is assigned to oxygen atoms movement along a line bisecting the T–O–T bond angle [43–45]. The spectrum is characterized by a broad band, as a consequence of Si/Al ordering. According to Sharma at all [46] substitution of $Al_{3p}$ for $Si_{4p}$ increases the localization of higher frequency modes and the Si–O–Al vibrations shifts toward lower frequencies. The peaks at 462 and 464 cm$^{-1}$ are also associated with T–O–T vibration.

The Raman peaks from 100 to 400 cm$^{-1}$ for both feldspars correspond to rotation-translation modes of the four-membered rings and lattice modes. The peak broadening and low intensity are consequence of a disordered arrangement of atoms Al and Si and the moves average Pb-position in structure. The Fourier map showed an anomalous electron-density distribution around the Pb site (Figs. 4 and 5). It indicates that the Pb-atoms are arranged in the two split positions, 4*i* on the plane *m* and general position 8*j*.

Based on the literature data [44–47] the mid to weak strength peaks in the 700–900 cm$^{-1}$ region belong to the deformation modes of the tetrahedra and are assigned to the Al−O and Al−O−Si valence vibrations. The Raman modes at 922 cm$^{-1}$ and 947 cm$^{-1}$ present in the spectra of Pb-feldspar$_{LTA}$ and Pb-feldspar$_{FAU}$ respectively can be attributed to the vibration stretching modes of the tetrahedra. The Raman spectra for both Pb-feldspar correspond well to those already published [43–47].

## 4. Conclusion

During the process of thermally induced phase transformation the Pb-exchange LTA and FAU zeolites formed the stable tetrahedral framework of the Pb-feldspar. The formation of an amorphous phase of Pb-LTA and Pb-FAU zeolites started approximately between 615 and 630 °C. At temperatures higher than 800 °C the Pb-zeolite precursors directly transform into the feldspar phase. The crystal structures of synthesized Pb-feldspar are observed in the space group *C*2/*m* (disorder structure).

The deviations of the bond length present in both feldspars are the consequence of the influence of the Pb cation. The crystal structure of the Pb-feldspar$_{LTA}$ was refined with following agreement factors: $R(F) = 6.39$, $R(B) = 6.91$, $Ch_2 = 2.07$ for the *C*2/*m*. The crystal structure of the Pb-feldspar$_{FAU}$ was refined with following agreement factors: $R(F) = 4.68$, $R(B) = 4.59$, $Ch_2 = 2.08$ for the *C*2/*m*.

## Acknowledgment

The authors are grateful for financial support of the Ministry of Education, Science and Technology of the Republic Serbia (Project numbers III-45012 and OI176016).

## References

[1] M.A. Subramanian, D. Corbin, R.D. Farlan, Mater. Res. Bull. 21 (1986) 1525–1532.
[2] P. Norby, Zeolites 10 (1990) 193–199.
[3] B. Hoghooghi, J. McKittrick, C. Butler, P. Desch, J. Non-Cryst. Solids 170 (3) (1994) 303–307.
[4] J. McKittrick, B. Hoghooghi, O.A. Lopez, J. Non-Cryst. Solids 197 (2–3) (1996) 170–178.
[5] G. Dell'Agli et al., Solid State Ionics 127 (3–4) (2000) 309–317.
[6] W. Schmidt, C. Weidenthaler, Microporous Mesoporous Mater. 48 (2001) 89–94.
[7] S. Esposito, C. Ferone, M. Pansini, L. Bonaccorsi, E. Proverbio, J. Eur. Ceram. Soc. 24 (9) (2004) 2689–2697.
[8] R. Dimitrijević, V. Dondur, A. Kremenović, Zeolites 16 (1996) 294–300.
[9] R. Dimitrijević, A. Kremenović, V. Dondur, M. Tomašević-Čanović, M. Mitrović, J. Phys. Chem. B 101 (1997) 3931–3936.
[10] B. Nedić, A. Kremenović, V. Dondur, R. Dimitrijevic, Cryst. Res. Technol. 43 (3) (2008) 266–272.
[11] C. Ferone et al., Chem. Mater. 14 (2) (2002) 797–803.
[12] B. Liguori, C. Ferone, S. Anaclerio, C. Colella, Solid State Ionics 179 (40) (2008) 2358–2364.
[13] C. Ferone, B. Liguori, A. Marocco, S. Anaclerio, M. Pansini, C. Colella, Microporous Mesoporous Mater. 134 (1–3) (2010) 65–71.
[14] U. Steinike, K. Jancke, E. Schreier, C. Staedler, W. Lutz, Cryst. Res. Technol. 30 (4) (1995) 559–569.
[15] P.H. Ribbe, Chemistry, Structure and Nomenclature of Feldspars, 2nd ed., In Mineralogical Society of America Reviews in Mineralogy, 1983.
[16] J.V. Smith, Feldspar Minerals, I Crystal Structure and Physical Properties, Springer-Verlag, Berlin, Heidelberg, New York, 1974.
[17] A. Kyono, M. Kimata, Mineral. Mag. 65 (4) (2001) 523–531.
[18] J. Deubener, M. Sternitzke, G. Müller, Am. Mineral. 76 (1991) 1620–1627.
[19] B.R. Doe, R.I. Tilling, Am. Mineral. 52 (3) (1967) 805–816.

[20] C.A. Sorrell, Am. Mineral. 47 (1962) 291–309.
[21] E. Bruno, G. Gazzoni, Periodico Mineral. 39 (1970) 245–253.
[22] E. Bruno, A. Facchinelli, Z. Kristallogr. 136 (1972) 296–304.
[23] J.B. Scheel, Z. Kristallogr. 133 (1971) 264–272.
[24] P. Benna, M. Tribaudino, E. Bruno, Am. Mineral. 81 (1996) 1337–1343.
[25] L. Rui, L. Anhuai, Q. Shan, Acta Geol. Sinica 80 (2) (2006) 175–179.
[26] P.W. Wang, L. Zhang, J. Non-Cryst. Solids 194 (1) (1996) 129–134.
[27] Ch. Baerlocher, W. Meier, D.H. Olson, Atlas of Zeolite Framework Types, Structure Commission of International Zeolite Association, Elsevier, Amsterdam, 2001.
[28] H.M. Rietveld, J. Appl. Crystallogr. 2 (1969) 65–71.
[29] J. Rodríguez-Carvajal, Physica B 192 (1993) 55–69.
[30] J. Rodríguez-Carvajal, Recent developments of the program FULLPROF.IUCr Commission on Powder Diffraction Newsletter, No. 26, pp. 12–19. <http://www.iucr.org/data/assets/pdf_file/0019/21628/cpd26.pdf 2001>.
[31] D. Balzar, J. Appl. Crystallogr. 25 (1992) 559–570.
[32] B. Antic, A. Kremenovic, A. Nikolic, M. Stoiljkovic, J. Phys. Chem. B 108 (2004) 12646–12651.
[33] M. Tribaudino, P. Benna, E. Bruno, Am. Mineral. 83 (1998) 159–166.
[34] P. Benna, M. Tribaudino, E. Bruno, Am. Mineral. 84 (1999) 120–129.
[35] R.D. Shannon, C.T. Prewitt, Acta Crystallogr. B25 (1969) 925–945.
[36] M. Skellern, R. Howie, E. Lachowski, J. Skakle, Acta Crystallogr. C 59 (2003) 11–14.
[37] H. Grundy, J. Ito, Am. Mineral. 59 (1319) (1974) 1319–1326.
[38] A.S. Wills, VaList. <www.ccp14.ac.uk>.
[39] R.E. Newnham, H. Megaw, Acta Crystallogr. 13 (1960) 303–312.
[40] P. Benna, E. Bruno, Am. Mineral. 86 (2001) 690–696.
[41] N.E. Brese, M. O'Keeffe, Acta Crystallogr. B47 (1991) 192–197.
[42] H. Megaw, Mineral. Mag. 32 (1959) 226–241.
[43] T.P. Mernagh, J. Raman Spectrosc. 22 (1991) 457–458.
[44] J.J. Freeman, A. Wang, K.E. Kuebler, B. Jolliff, L. Haskin, Can. Mineral. 46 (2008) 1477–1500.
[45] B. Velde, H.J. Boyer, J. Geophys. Res. 90 (1985) 3675–3682.
[46] S.K. Sharma, B. Simons, H.S. Yoder, Am. Mineral. 68 (1983) 113–1125.
[47] P. McMillan, B. Piriou, A. Navrotsky, Geochim. Cosmochim. Acta 46 (1982) 2012–2037.